
Dressing of the Charge Carriers in High- T_c Superconductors

J. Fink^{1,2}, S. Borisenko¹, A. Kordyuk^{1,3}, A. Koitzsch¹, J. Geck¹,
V. Zabolotnyy¹, M. Knupfer¹, B. Büchner¹, and H. Berger⁴

¹ Leibniz Institute for Solid State and Materials Research Dresden, P.O. Box
270016, 01171 Dresden, Germany
J.Fink@ifw-dresden.de

² Ames Laboratory, Iowa State University, Ames, Iowa 50011, USA

³ Institute of Metal Physics of the National Academy of Sciences of Ukraine,
03142 Kyiv, Ukraine

⁴ Institut de Physique de la Matière Complex, Ecole Polytechnique Fédérale de
Lausanne, 1015 Lausanne, Switzerland

Abstract. In this contribution we first present a short introduction into the lattice structure, the phase diagram and the electronic structure of high- T_c superconductors. Then we explain the principles of angle-resolved photoemission spectroscopy (ARPES) and the influence of the dressing of the charge carriers, which is normally described by the complex self-energy function, on the spectral function in the normal and the superconducting state. Finally we review our recent ARPES results on high- T_c superconductors at various \mathbf{k} -points in the Brillouin zone near the Fermi surface. Information on the dressing of the charge carriers, i.e., on the effective mass and the scattering length, is obtained as a function of doping concentration, temperature, momentum and energy. The strong renormalization of the bandstructure due to the dressing can be explained in terms of a coupling to a continuum of spin fluctuations and in the superconducting state by an additional coupling to a triplet exciton excitation. Possibly, this dressing is related to the glue for the pair formation in cuprate superconductors.

11.1 Introduction

One hundred years ago, in the first of five famous papers [1] of his *annus mirabilis*, Albert Einstein postulated the dual nature of light, at once particle and wave, and thereby explained among other phenomena the photoelectric effect, originally discovered by H. Hertz [2]. This work of Einstein was also singled out by the Nobel committee in 1921. The photoelectric effect has since become the basis of one of the most important techniques in solid state research. In particular, angle-resolved photoemission spectroscopy (ARPES), first applied by Gobel et al. [3], has developed to *the* technique to determine

the bandstructure of solids. During the last decade, both the energy and the angular resolution of ARPES has increased by more than one order of magnitude. Thus it is possible to measure the dispersion very close to the Fermi level, where the spectral function, which is measured by ARPES, is renormalized by many-body effects such as electron–phonon, electron–electron, or electron–spin interactions. The mass enhancement due to such effects leads to a reduced dispersion and the finite life-time of the quasi-particles leads to a broadening of the spectral function. Thus the increase in resolution, achieved by new analyzers using two-dimensional detectors, together with new photon sources provided by undulators in 3rd generation synchrotron storage rings and new cryo-manipulators have opened a new field in ARPES: the determination of the low-energy many-body properties of solids which is termed very often the “dressing” of the charge carriers.

In high- T_c superconductors (HTSCs) discovered by Bednorz and Müller [4] the many-body effects are supposed to be particularly strong since these doped cuprates are close to a Mott–Hubbard insulator or, to be more precise, to a charge-transfer insulator [5]. Since in the normal and the superconducting state the renormalization effects are strong, the HTSCs are a paradigm for the new application of ARPES. Moreover, since in these compounds the mass enhancement and the superconducting gap are large, they can be measured using ARPES even without ultra-high resolution.

On the other hand, the understanding of the renormalization effects in the HTSCs is vital for the understanding of the mechanism of high- T_c superconductivity, since the dressing of the charge carriers may be related with the glue forming the Cooper pairs. Up to now there is no widely accepted microscopic theory, although the phenomenon has been discovered already 20 years ago. Similar to the conventional superconductors, before the development of a microscopic theory for the mechanism of superconductivity, first one has to understand the many-body effects in the normal state of these highly correlated systems. ARPES plays a major role in this process. Not only can it determine the momentum dependent gap. It is at present also the only method which can determine the momentum dependence of the renormalization effects due to the interactions of the charge carriers with other degrees of freedom.

In this contribution we review ARPES results on the dressing of the charge carriers in HTSCs obtained by our spectroscopy group. There are previous reviews on ARPES studies of HTSCs [6–8], which complement what is discussed here. Similar results are presented by Johnson and Valla and by Takahashi et al. in this volume.

11.2 High- T_c Superconductors

11.2.1 Structure and Phase Diagram

It is generally believed that superconductivity is associated with the two-dimensional CuO_2 planes shown in Fig. 11.1(a). In these planes Cu is divalent, i.e., Cu has one hole in the $3d$ shell. The CuO_2 planes are separated by block layers formed by other oxides (see Fig. 11.1(b)). Without doping, the interacting CuO_2 planes in the crystal form an antiferromagnetic lattice with a Néel temperature of about $T_N = 400$ K. By substitution of the ions in the block layers, it is possible to dope the CuO_2 planes, i.e., to add or to remove electrons from the CuO_2 planes. In this review we focus on hole doped systems. With increasing hole concentration and increasing temperature, the long-range antiferromagnetism disappears (see the phase diagram in Fig. 11.1(c)) but one knows from inelastic neutron scattering that spin fluctuations still exist at higher dopant concentrations and higher temperatures.

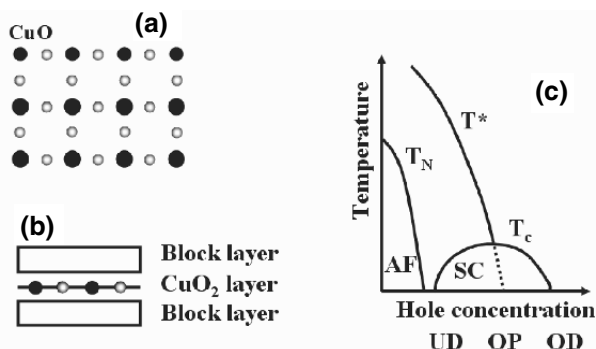


Fig. 11.1. (a) CuO_2 plane; (b) CuO_2 plane between block layers; (c) schematic phase diagram of hole-doped cuprates

With increasing dopant concentration the insulating properties transform into metallic ones and there is a high- T_c superconducting range. This range is normally divided into an underdoped (UD), an optimally doped (OP) and an overdoped (OD) region. Not only the superconducting state but also the normal state is unconventional. In the UD range there is a pseudogap between the T^* line and the T_c line. There are various explanations for the pseudogap [9]: preformed pairs which have no phase coherence, spin density waves, charge density waves, or the existence of a hidden order, caused, e.g. by circulating currents [10]. At low temperatures in the OP region the T^* line is very often related to a quantum critical point near the OP region. Possibly related to this quantum critical point, in the OP range, the normal state shows rather strange properties such as a linear temperature dependence of the resistivity

over a very large temperature range or a temperature dependent Hall effect. Only in the OD range the system behaves like a normal correlated metal showing for example a quadratic temperature dependence of the resistivity.

11.2.2 Electronic Structure

In the following we give a short introduction into the electronic structure of cuprates. We start with a simple tight-binding bandstructure of a CuO_2 plane using for the beginning three hopping integrals, one between 2 neighboring Cu sites along the Cu-O bonding direction (t), one for a hopping to the second nearest Cu neighbor along the diagonal (t'), and one for the hopping to the third nearest neighbor (t''). The corresponding bandstructure is given by

$$E(\mathbf{k}) = \Delta\epsilon - 2t[\cos(k_x a) + \cos(k_y a)] + 4t' \cos(k_x a) \cos(k_y a) - 2t''[\cos(2k_x a) + \cos(2k_y a)] \quad (11.1)$$

where a is the length of the unit cell and $\Delta\epsilon$ fixes the Fermi level. This two-dimensional bandstructure is displayed in Fig. 11.2(a) for $t'/t = -0.3$, a value which is obtained from bandstructure calculations [11], and both t'' and $\Delta\epsilon$ equal to zero. It has a minimum in the center (Γ) and maxima at the corners of the Brillouin zone (e.g. at $(k_x, k_y) = (\pi, \pi)/a \equiv (\pi, \pi)$). Furthermore there are saddle points, e.g. at $(k_x, k_y) = (\pi, 0)$. In the undoped system there is one hole per Cu site and therefore this band should be half filled. This leads to a Fermi level just above the saddle points (see Fig. 11.2(a)). The Fermi surface consists of rounded squares around the corners of the Brillouin zone (see Fig. 11.2(b)). Upon hole doping the Fermi level moves towards the saddle point. It is interesting that for vanishing t' the Fermi surface would be quadratic and there would be no parallel sections (which could lead to a nesting) along x or y but along the diagonal. There are two special points on the Fermi surface (see Fig. 11.2(b)), which are also at the focus of most of the ARPES studies on HTSCs. There is the nodal point at the diagonal (N in Fig. 11.2(b)), where the superconducting order parameter is zero and the antinodal point (where the $(\pi, 0)-(\pi, \pi)$ line cuts the Fermi surface), where the superconducting order parameter is believed to reach a maximum (AN in Fig. 11.2(b) [12, 13]).

In many cuprates there is not just a single but several CuO_2 planes between the block layers. In these systems the CuO_2 planes are separated by additional ionic layers. This is illustrated for a bilayer system in Fig. 11.2(c). Such a bilayer system is for example $\text{Bi}_2\text{Sr}_2\text{CaCu}_2\text{O}_8$ which is the Drosophila for ARPES studies of HTSCs. In this compound the block layers are composed of BiO and SrO planes, while the ionic layer separating the two CuO_2 planes consist of Ca^{2+} layers. Doping is achieved in this compound by additional O atoms in the block layers. In those bilayer systems there is an interaction between the two adjacent CuO_2 planes which leads to a finite hopping integral t_\perp . This causes an additional term in the tight-binding calculations

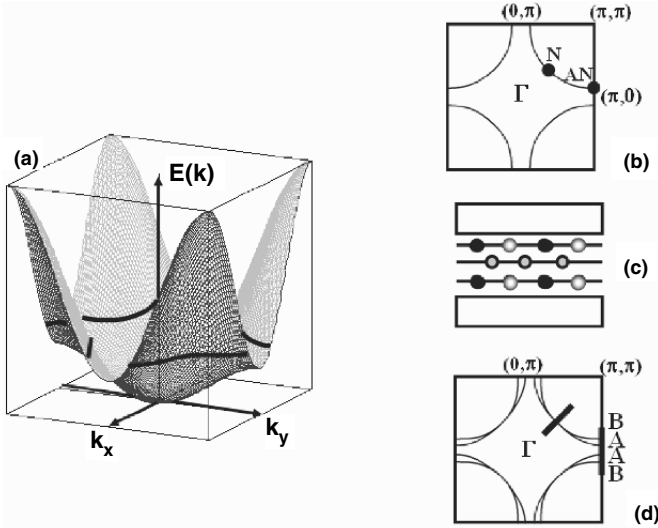


Fig. 11.2. (a) Tight-binding bandstructure of the CuO_2 plane; (b) Fermi surface of a CuO_2 plane. N: nodal point, AN: antinodal point; (c) bilayer system between block layers composed of two CuO_2 planes separated by one ionic layer; (d) Fermi surfaces of a bilayer system, B(A): (anti)bonding band. *Thick solid lines:* \mathbf{k} values along which most of the present ARPES studies have been performed

$$E(\mathbf{k})_{\perp} = \pm t_{\perp} [\cos(k_x a) - \cos(k_y a)]^2 / 4 \quad (11.2)$$

leading to a splitting into a bonding and an antibonding band. This splitting is small at the nodal point [14] and it is largest at the antinodal point. In Fig. 11.2(d) we have illustrated this splitting of the Fermi surface caused by the interaction of the two CuO_2 planes.

The independent particle picture, describing just the interactions with the ion lattice and the potential of a homogeneous conduction electron distribution, is of minor use for the undoped systems since we know that those are not metallic but insulating. This comes from the Coulomb interaction U of two holes on the same Cu site which prohibits hopping of holes from one Cu site to the other. It causes the insulating behavior of undoped and slightly doped cuprates. The large on-site Coulomb repulsion of two holes on a Cu site is also responsible for the fact that the additional holes produced upon doping are formed on O sites [15]. The 2 eV energy gap is then a charge-transfer gap [5] between O $2p$ and Cu $3d$ states. Only when more and more holes are introduced into the CuO_2 planes is hopping of the holes possible and correlation effects get less important.

11.3 Angle-resolved Photoemission Spectroscopy

11.3.1 Principle

In photoemission spectroscopy monochromatic light with an energy $h\nu$ is shined onto a surface of a solid and the intensity as well as the kinetic energy, E_{kin} , of the outgoing photoelectrons is measured. Using the explanation of the photoelectric effect [1] one can obtain the binding energy of the electrons in the solid:

$$E_B = h\nu - \Phi - E_{kin} \equiv -E . \quad (11.3)$$

Here Φ is the workfunction. The charge carriers in HTSCs show a quasi-two-dimensional behavior. When the surface is parallel to the CuO_2 planes, the momentum $\hbar k_{\parallel}$ of the photoelectron is conserved when passing through the surface and thus this momentum is determined by the projection of the total momentum of the photoelectron to the surface:

$$\hbar k_{\parallel} = \sqrt{2mE_{kin}} \sin \theta . \quad (11.4)$$

Here θ is the angle between the direction of the photoelectron in the vacuum and the surface normal.

There are numerous treatises of the photoelectron process in the literature where the limitations of the models describing it are discussed [16]. They are not repeated in this contribution. Rather the essential points for the analysis of ARPES studies on the dressing of the charge carriers in HTSCs are restated. It is assumed that the energy and momentum dependence of the photocurrent in ARPES studies can be described by

$$I(E, \mathbf{k}) \propto M^2 A(E, \mathbf{k}) f(E) + B(E, \mathbf{k}) \quad (11.5)$$

where $M = \langle \psi_f | H' | \psi_i \rangle$ is a matrix element between the initial and the final state and H' is a dipole operator. $A(E, k)$ is the spectral function which is the essential result in ARPES studies. $f(E) = 1/[\exp(E/k_B T) + 1]$ is the Fermi function which takes into account that only occupied states are measured and $B(E, \mathbf{k})$ is an extrinsic background coming from secondary electrons. For a comparison of calculated data with experimental data, the former have to be convoluted with the energy and momentum resolution.

The dynamics of an electron in an interacting system can be described by a Green's function [17]

$$G(E, \mathbf{k}) = \frac{1}{E - \epsilon_{\mathbf{k}} - \Sigma(E, \mathbf{k})} . \quad (11.6)$$

$\Sigma(E, \mathbf{k}) = \Sigma'(E, \mathbf{k}) + i\Sigma''(E, \mathbf{k})$ is the complex self-energy function which contains the information on the dressing, i.e., on what goes beyond the independent-particle model. $\epsilon_{\mathbf{k}}$ gives the dispersion of the bare particles without many-body interactions. The spectral function can be expressed [18, 19] by

$$A(E, \mathbf{k}) = -\frac{1}{\pi} \text{Im}G(E, \mathbf{k}) = -\frac{1}{\pi} \frac{\Sigma''(E, \mathbf{k})}{[E - \epsilon_{\mathbf{k}} - \Sigma'(E, \mathbf{k})]^2 + [\Sigma''(E, \mathbf{k})]^2} \quad (11.7)$$

For $\Sigma = 0$, i. e., for the non-interacting case, the Green's function and thus the spectral function is a delta function at the bare-particle energy $\epsilon_{\mathbf{k}}$. Taking interactions into account, the spectral function given in Eq. (11.7) is a rather complicated function. On the other hand, in many cases only local interactions are important which leads to a \mathbf{k} -independent or weakly \mathbf{k} -dependent self-energy function. Furthermore, in the case of not too strong interactions, often quasi-particles with properties still very close to the bare particles, can be projected out from the spectral function. To perform this extraction one expands the complex self-energy function around the bare particle energy $\epsilon_{\mathbf{k}}$: $\Sigma(E) \approx \Sigma(\epsilon_{\mathbf{k}}) + \partial\Sigma(E)/\partial E|_{E=\epsilon_{\mathbf{k}}}(E - \epsilon_{\mathbf{k}})$. Very often one introduces the coupling function $\lambda(\epsilon_{\mathbf{k}}) = -\partial\Sigma'(E)/\partial E|_{E=\epsilon_{\mathbf{k}}}$ and the renormalization function $Z(\epsilon_{\mathbf{k}}) = 1 + \lambda$. Note that most unfortunately the *renormalization function* as used here is defined in the literature as $Z(\epsilon_{\mathbf{k}}) = 1 + \lambda$ whereas the *renormalization constant* $Z(\epsilon_{\mathbf{k}} = 0)$ is given by $Z(\epsilon_{\mathbf{k}} = 0) = [1 + \lambda(\epsilon_{\mathbf{k}} = 0)]^{-1}$. Neglecting the partial derivative of $\Sigma''(E)$ one obtains for the spectral function

$$A(E, \mathbf{k})_{coh} = -\frac{1}{\pi} Z(\epsilon_{\mathbf{k}})^{-1} \frac{Z(\epsilon_{\mathbf{k}})^{-1} \Sigma''(\epsilon_{\mathbf{k}})}{[E - \epsilon_{\mathbf{k}} - Z(\epsilon_{\mathbf{k}})^{-1} \Sigma'(\epsilon_{\mathbf{k}})]^2 + [Z(\epsilon_{\mathbf{k}})^{-1} \Sigma''(\epsilon_{\mathbf{k}})]^2} \quad (11.8)$$

This is the coherent fraction of the spectral function and its spectral weight is given by Z^{-1} . It is called coherent because it describes a (quasi-)particle which is very similar to the bare particle. Instead of a delta-function we have now a Lorentzian. The energy of the quasi-particle is determined by the new maximum of the spectral function which occurs at $E = \epsilon_{\mathbf{k}} - Z^{-1} \Sigma'(\epsilon_{\mathbf{k}})$. The life-time of the quasi-particle is determined in a cut at constant \mathbf{k} by the FWHM of the Lorentzian which is given by $\Gamma = 2Z^{-1} \Sigma''(\epsilon_{\mathbf{k}})$.

Close to the Fermi we can assume that the real part of the self-energy is linear in energy, i.e., $\Sigma'(\epsilon_{\mathbf{k}}) = -\lambda\epsilon_{\mathbf{k}}$, with λ being a constant. Then also $Z(0)$ is a constant. We reiterate that in many contributions in the literature (also in all other contributions of this volume where the renormalization constant Z is used!) this renormalization constant $Z(0)$ is termed $1/Z$. For the renormalized energy of the quasi-particle, we now obtain $E_{\mathbf{k}} = \epsilon_{\mathbf{k}}/(1 + \lambda)$. Thus close to the Fermi level we have in the case of a linear real part of the self-energy a renormalization by a factor of $1 + \lambda$ or in other words, due to the interactions we have for the coherent quasi-particles a mass enhancement $m^* = (1 + \lambda)m$.

The incoherent part of the spectral function, the spectral weight of which is given by $1 - Z^{-1}$, contains all the spectral weight that cannot be described by the Lorentzian close to the bare particle energy, e.g., satellites. Z^{-1} also determines the size of the jump at \mathbf{k}_F of the momentum distribution $n(k)$, which can be calculated from the energy integral of the spectral function $A(E, \mathbf{k})$. Thus if the jump in $n(k)$ comes to zero, at this very point the quasi-particle weight Z^{-1} vanishes logarithmically as one approaches the Fermi level. For such an electron liquid the term "marginal" Fermi liquid [20] has

been introduced. This is related to another condition for the existence of (coherent) quasi-particles [21, 22]. The finite lifetime implies an uncertainty in energy. Only if this uncertainty is much smaller than the binding energy ($\Sigma''/E \rightarrow 0$) the particles can propagate coherently and the concept of quasi-particles has a physical meaning.

In principle, performing constant- \mathbf{k} scans, commonly called energy distribution curves (EDCs), one can extract the spectral function along the energy axis and using Eq. (11.7) one can derive the complex self-energy function. In reality there is a background, the exact energy dependence of which is not known. In addition, close to the Fermi energy there is the energy-dependent Fermi function. These problems are strongly reduced when performing constant-energy scans, usually called momentum distribution curves (MDCs) [23]. Close to the Fermi level the bare particle bandstructure can be expanded as $\epsilon_k = v_F \hbar(k - k_F)$. Assuming again a weakly \mathbf{k} -dependent $\Sigma(E, \mathbf{k})$, the spectral function along the particular \mathbf{k} -direction is a Lorentzian (see Eq. (11.7)). The width is given by $\Sigma''/v_F \hbar$ and from the shift relative to the bare particle dispersion one can obtain the real part Σ' . This evaluation is much less dependent on a weakly \mathbf{k} -dependent background and on the Fermi function.

11.3.2 Spectral Function in the Normal State

In a real solid there are several contributions to the self-energy. The important ones, related to inelastic scattering processes can be reduced to contributions which are related to bosonic excitations (see Fig. 11.3). In the case where the boson is a particle-hole excitation, which is depicted in Fig. 11.3(a), a photoelectron hole is filled by a transition from a higher energy level and the energy is used to excite an Auger electron to a state above the Fermi level. The final state is thus a photoelectron hole scattered into a higher state plus an electron-hole pair. For a normal Fermi liquid of a three-dimensional solid at $T = 0$ phase space arguments and the Pauli principle lead to the complex self-energy function $\Sigma = \alpha E - i\beta E^2$. In a two-dimensional solid the imaginary

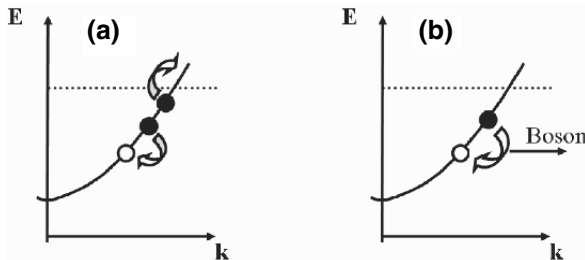


Fig. 11.3. Bosonic excitations contributing to the finite lifetime of a photohole in metallic solids. (a) electron-hole excitations, (b) discrete bosonic mode. The *dashed line* corresponds to the Fermi level.

part of Σ changes from a quadratic energy dependence to $\beta' E^2 \ln |E/E_F|$ [24] which is similar to the 3D case only as long as E is much smaller than the bandwidth. Increasing the interactions more and more, associated with a reduction of Z^{-1} , changes the self-energy function. For $Z^{-1} = 0$ where the spectral weight of the quasi-particles disappears one reaches the above mentioned marginal Fermi liquid [20]. In this case the self-energy is given by $\Sigma = \lambda_{MFL}[E \ln |x/E_c| + i(\pi/2)x]$ where $x = \max(E, k_B T)$ and E_c is a cutoff energy taking into account the finite width of the conduction band. This self-energy function is a phenomenological explanation, among others, of the linear temperature dependence of the resistivity observed in optimally doped HTSCs, since the imaginary part of the self-energy and thus the inverse scattering rate is linear in T .

Besides the particle-hole excitations described above, the photohole may be scattered to higher (lower) energies by the emission (absorption) of a discrete boson. This is illustrated in Fig. 11.3(b) for the emission of a bosonic excitation. Such discrete bosonic excitations may be phonons, spin excitations, plasmons, excitons, etc. The relevant excitations are listed in Table 11.1 together with their characteristic energies in optimally doped HTSCs.

Table 11.1. Bosonic excitations which couple to the charge carriers together with their characteristic energies in HTSCs

| System | Excitations | Characteristic energy(meV) |
|---------------------|-------------|----------------------------|
| ion lattice | phonons | 90 |
| spin lattice/liquid | magnons | 180 |
| e-liquid | plasmons | 1000 |

The self-energy function for a coupling of the charge carriers to a bosonic mode for the case that the energy of the mode is much smaller than the band width has been treated by Engelsberg and Schrieffer [25]. The assumption of a strong screening of the bosonic excitations is probably adequate for the doped HTSCs but probably not for the undoped or slightly doped parent compounds [26,27]. In the well-screened case, Σ'' is zero up to the mode energy Ω_0 . This is immediately clear from Fig. 11.3(b) since the photohole can only be filled when the binding energy is larger than Ω_0 . Σ'' is constant above the mode energy (see Fig. 11.4(b)). Performing the Kramers–Kronig transformation one obtains Σ' , which is given by $\Sigma' = (\lambda\Omega_0/2) \ln |(E+\Omega_0)/(E-\Omega_0)|$ (see Fig. 11.4(a)). It shows a logarithmic singularity at the mode energy, Ω_0 . At low energies there is a linear energy dependence of Σ' and the slope determines the coupling constant λ . In this model it is related to the imaginary part of the self-energy function $\Sigma''(|E| > \Omega_0) \equiv \Sigma''(-\infty)$, by $\lambda = -\Sigma''(-\infty)/(\pi\Omega_0/2)$. From this it is clear that for a given Ω_0 both λ and $\Sigma''(-\infty)$ are a measure of the coupling strength to the bosonic mode.

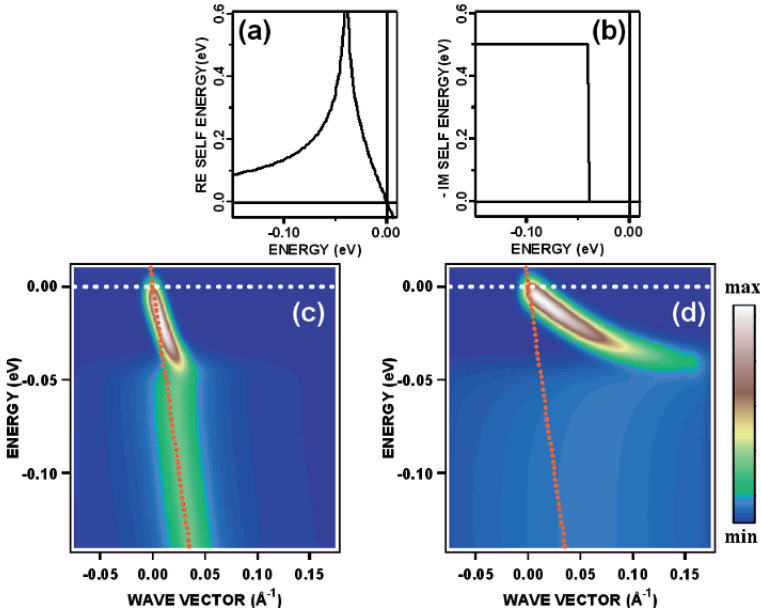


Fig. 11.4. Real part (a) and imaginary part (b) of the self-energy function for a coupling to a mode $\Omega_0 = 40$ meV and a coupling constant $\lambda = 8$. Calculated spectral function $A(E, \mathbf{k})$ for $\lambda = 1$ (c) and $\lambda = 8$ (d) in the normal state

In Fig. 11.4(c) and (d) we have displayed the calculated spectral function for $\lambda = 1$ and $\lambda = 8$, respectively. Compared to the bare particle dispersion, given by the red dashed line, for $|E| < \Omega_0$ there is a mass renormalization, i.e., a reduced dispersion and no broadening, except the energy and momentum resolution broadening, which was taken to be 5 meV and 0.005 \AA^{-1} , respectively. For $|E| > \Omega_0$, there is a back-dispersion to the bare particle energy. Moreover, there is a broadening due to a finite Σ'' , increasing with increasing λ . For large λ , the width for constant E scans is, at least up to some energy, larger than the energy of the charge carriers and therefore they can be called incoherent (see Subsect. 11.3.2) in contrast to the energy range $|E| < \Omega_0$ or at very high binding energies, where the width is much smaller than the binding energy and where they are coherent [25]. The change in the dispersion is very often termed a “kink” but looking closer at the spectral function, in particular for high λ , it is a branching of two dispersion arms.

11.3.3 Spectral Function of Solids in the Superconducting State

For the description of the spectral function in the superconducting state, two excitations have to be taken into account: the electron-hole and the pair excitations. This leads to a (2×2) Green’s function [28]. Usually the complex renormalization function

$$Z(E, \mathbf{k}) = 1 - \Sigma(E, \mathbf{k})/E, \quad (11.9)$$

is introduced. For the one-mode model, the self-energy of the superconducting state corresponds to the self-energy of the normal state in which Ω_0 is replaced by $\Omega_0 + \Delta$. This can be easily seen from Fig. 11.3(b) and assuming a gap opening with the energy Δ . The coupling constant in the superconducting state, λ_{sc} , is related to the renormalization function by $\lambda_{sc} = Z(0) - 1$. For the Auger process shown in Fig. 11.3(a) the onset of the scattering rate is at 3Δ . The reason for this is that the bosonic (e-h) excitations have in this case a lower limit of 2Δ . The complex spectral function is given by [29]

$$A(E, \mathbf{k}) = -\frac{1}{\pi} \text{Im} \frac{Z(E, \mathbf{k})E + \epsilon_{\mathbf{k}}}{Z(E, \mathbf{k})^2(E^2 - \Delta(E, \mathbf{k})^2) - \epsilon_{\mathbf{k}}^2}. \quad (11.10)$$

In general, $\Delta(E, \mathbf{k})$ is also a complex function. In Fig. 11.5 we show for the one-mode model the calculated spectral function in the superconducting state using the same energy and momentum resolutions and the same mode energy as before. The imaginary part of Δ was neglected and the real part was set to 30 meV. One clearly realizes the BCS-Bogoliubov-like back-dispersion at the gap energy Δ and besides this, a total shift of the dispersive arms by the gap energy. Thus the branching energy occurs at $\Omega_0 + \Delta$.

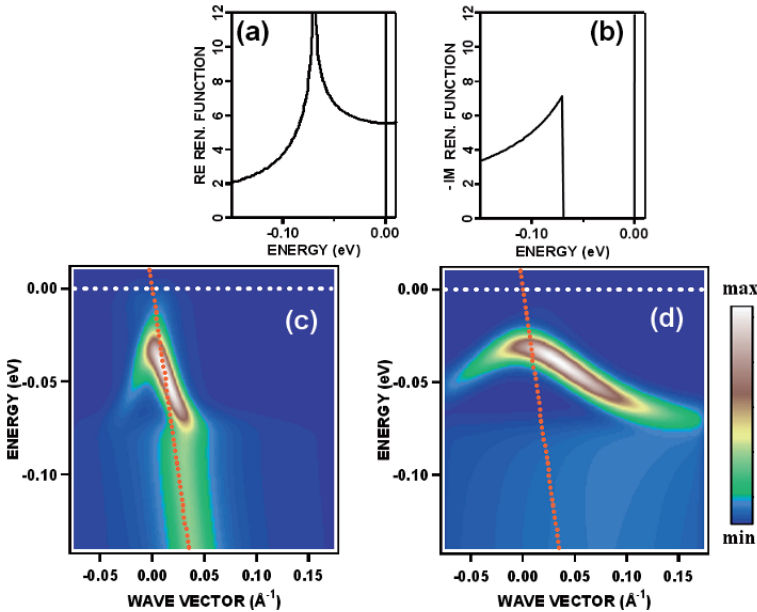


Fig. 11.5. The real part (a) and imaginary part (b) of the renormalization function $Z(E)$ for $\Omega_0 = 40$ meV, $\Delta = 30$ meV, and $\lambda_{sc} = 5$. Spectral function $A(E, k)$ for a coupling constant $\lambda_{sc} = 1$ (c) and $\lambda_{sc} = 5$ (d) in the superconducting state

Looking at the phase diagram in Fig. 11.1(c) it is clear that the HTSCs are very close to a transition into a Mott-insulating state and therefore we expect a large fraction of incoherent spectral weight in the normal state. This, however changes when going into the superconducting state where for $\min(\Delta + \Omega_0, 3\Delta) > |E| > \Delta$ the incoherent states are transformed into coherent ones. The reason for this is that in the superconducting state a gap opens for Σ'' for $|E| < 3\Delta$ (e-h scattering rate) or for $|E| < \Omega_0 + \Delta$ (bosonic scattering rate).

The dispersion is given by [30]:

$$[\text{Re}Z(E, \mathbf{k})]^2 [E^2 - \Delta(E, \mathbf{k})^2] - \epsilon_{\mathbf{k}}^2 = 0. \quad (11.11)$$

In the conventional superconductors the mode energy is much larger than the gap and therefore for $|E|$ slightly larger than Δ , Z , and thus λ_{sc} , are constant. In this case Eq. (11.11) yields for the maxima of the spectral function

$$E = \sqrt{\Delta^2 + \epsilon_{\mathbf{k}}^2 / (1 + \lambda_{sc})^2}. \quad (11.12)$$

For HTSC the gap is comparable to the mode energy and therefore Eq. (11.12) is no longer valid and the full Eq. (11.11) should be used to fit the dispersion. Then λ_{sc} is related to the normal state λ_n (from $\lambda_n = (Z(0) - 1)|_{\Delta=0}$) by $\lambda_n = \lambda_{sc}(\Omega_0 + \Delta)/\Omega_0$. It is this λ_n which should be considered when comparing the coupling strength of the charge carriers to a bosonic mode of HTSCs and conventional superconductors.

When one measures an EDC at k_F a peak is observed followed by a dip and a hump. Such an energy distribution is well known from tunnelling spectroscopy in conventional superconductors which was explained in terms of a coupling of the electrons to phonons. A closer inspection indicates for the one-mode-model that at k_F the peak is followed by a region of low spectral weight and a threshold, which appears at $\Omega_0 + \Delta$. Far away from k_F this threshold is not contaminated by the tails of the peak.

11.3.4 Experimental

During the last decade ARPES has experienced an explosive period of qualitative and quantitative improvements. Previously ARPES was performed by rotating the analyzer step by step. In this way an enormous amount of information was lost because only one angle of the emitted photoelectrons was recorded. The development of the so-called ‘‘angle mode’’ [31], applied in the new generation of Gammadata-Scienta analyzers, allows the simultaneous recording of both an energy and an angle range. This was achieved by a multielement electrostatic lens system, by which each photoemission angle was imaged to a different spot of the entrance slit of the a hemispherical, electrostatic deflection analyzer. This angular information is then transferred to the exit of the analyzer and the energy and angle dispersion is recorded

by a two-dimensional detector consisting of a microchannel plate, a phosphor plate, and a charge coupled device detector. This caused an improvement both of the energy and the momentum resolution by more than one order of magnitude and an enormous improvement of the detection efficiency, leading to a very strong reduction of measuring time. But not only new analyzers and detectors lead to a huge progress of the ARPES technique. Also new photon sources such as undulators in synchrotron storage rings [32], new microwave driven He discharge lamps, and new cryo-manipulators contributed to the rapid development of the method.

The measurements presented in this contribution were performed with Gammadata-Scienta SES 200 and 100 analyzers using the above-mentioned angle mode. The photon sources used were a high-intensity He resonance Gammadata VUV 5000 lamp or various beamlines, delivering linearly or circularly polarized light in a wide energy range between 15 and 100 eV: the U125/1 PGM beamline at BESSY [33], the 4.2R beamline “Circular Polarization” at ELETTRA, or the beamline SIS at the SLS. The angular rotation of the sample was achieved by a purpose built high-precision cryo-manipulator which allows the sample to be cooled to 25 K and a computer-controlled angular scanning around three perpendicular axes in a wide range of angles with a precision of 0.1° . The energy and the angle/momentum resolutions were set in most cases in the ranges 8-25 meV and $0.2^\circ/0.01 - 0.02 \text{ \AA}^{-1}$, respectively, which is a compromise between energy and momentum resolution and intensity.

Almost all results presented in this review were obtained from high-quality and well characterized single crystals of $(\text{Bi,Pb})_2\text{Sr}_2\text{CaCu}_2\text{O}_{8+\delta}$ (Bi2212). The reason for this is the following. There is only van der Waals bonding between two adjacent BiO planes and therefore it is easy to cleave the crystals. Upon cleaving, no ionic or covalent bonds are broken which would lead to polar surfaces and to a redistribution of charges at the surface. Moreover, we know from bandstructure calculations that among all HTSCs, the Bi-compounds have the lowest k_z dispersion, i.e., they are very close to a two-dimensional electronic system. This is very important for the evaluation of the ARPES data. Probably on all other HTSCs, upon cleaving there is a redistribution of charges and possibly a suppressed superconductivity at the surface. The bilayer system of the Bi-HTSC family is complicated by the existence of two bands at the Fermi surface. On the other hand, it is that system where the whole superconducting range from the UD to the OD range can be studied. The system without Pb has a further complication. It has a superstructure along the b -axis leading in ARPES to diffraction replicas which complicate the evaluation of the data [34,35]. In order to avoid this, about 20% of the Bi ions were replaced by Pb which leads to superstructure-free samples.

The potential of the new generation ARPES technique is illustrated in Fig. 11.6 where we show room temperature data of OP Bi2212 in the three-dimensional (E, k_x, k_y) space. The fourth dimension is symbolized by the color scale, representing the photoelectron intensity. The right front plane of the

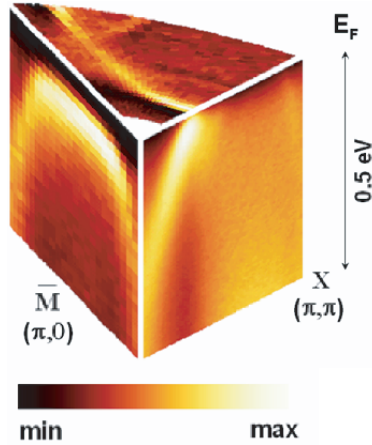


Fig. 11.6. Photoelectron intensity of a $(\text{Bi,Pb})_2\text{Sr}_2\text{CaCu}_2\text{O}_{8+\delta}$ single crystal in the three-dimensional (E, k_x, k_y) space measured at room temperature by ARPES

section shown in Fig. 11.6 was taken simultaneously by setting the \mathbf{k} -vector parallel to the $\Gamma - (\pi, \pi)$ direction. Then the sample was turned step by step until the \mathbf{k} -vector was parallel to the $\Gamma - (\pi, 0)$ direction thus sampling 100000 data points of the whole section.

Such a “piece of cake” can be cut along different directions. A horizontal cut at the Fermi level yields the Fermi surface. A vertical cut along a certain \mathbf{k} -direction yields the “bandstructure” (the bare particle dispersion plus the renormalization) along this direction. In these data, the essential points of the bandstructure shown in Fig. 11.2 are reproduced. Along the $\Gamma - (\pi, \pi)$ direction there is a crossing of the Fermi level at the nodal point (close to $(\pi/2, \pi/2)$). Along the $\Gamma - (\pi, 0)$ direction there is no crossing of the Fermi level but the saddle point is realized just below E_F .

11.4 The Bare-particle Dispersion

In order to extract the dressing of the charge carriers due to the many-body effects from the ARPES data, one has to know the bare-particle dispersion, i.e., the dispersion which is determined only by the interaction with the ions and the potential due to a homogeneous conduction electron distribution. We have suggested three different ways to obtain the bare-particle band structure.

The first one starts with the Fermi surface measured by ARPES. How to measure those has been already described in Subsect. 11.3.4. In Fig. 11.7 we show ARPES measurements of the Fermi surface of Bi2212 for various dopant concentrations [36]. Using a commonly employed empirical relation [37] between T_c and the hole concentration, x , determined from chemical analysis,

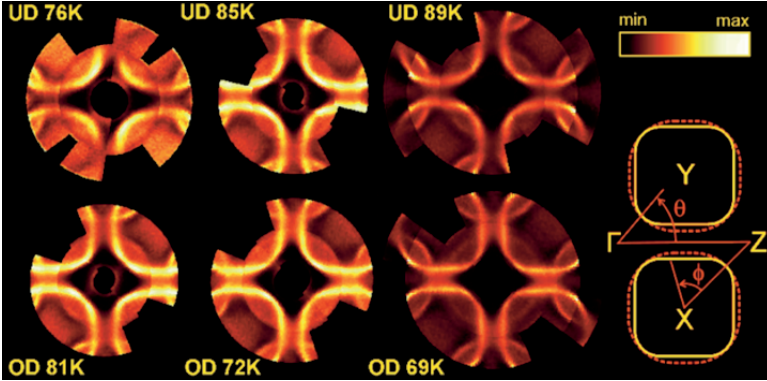


Fig. 11.7. Fermi surfaces of $(\text{Bi,Pb})_2\text{Sr}_2\text{CaCu}_2\text{O}_{8+\delta}$ having various dopant concentrations and T_c (indicated in the panels in units of K) measured by ARPES at room temperature. *Upper row:* underdoped (UD) samples, *lower row:* overdoped (OD) samples

the measured samples cover a doping range of $x = 0.12$ to 0.22 . The measurements were performed at room temperature.

Before we come to the evaluation of the bare-particle dispersion, we make some remarks on the character of the measured Fermi surfaces. Firstly, the topology does not change, which means that within the studied doping range there is no transition from a hole-like to an electron-like surface. Secondly, the shape of the Fermi surface around (π, π) changes from being quite rounded at low doping to taking on the form of a square with well rounded corners at higher doping. This is exactly what is expected within a rigid-band approximation and looking at Fig. 11.2. At low doping we are far away from the saddle point and we expect a more rounded Fermi surface. At higher doping we move E_F closer to the saddle point leading to a more quadratic Fermi surface. Thirdly, in underdoped samples, there is an intensity reduction close to $(\pi, 0)$ although the intensities are normalized to the total intensity along the particular \mathbf{k} -direction to reduce effects due to the \mathbf{k} -dependence of the matrix element in Eq. (11.5). This reduction in spectral weight is related to the formation of the pseudo-gap below T^* , which is above room temperature in the underdoped samples. This can be treated as a formation of arcs around the nodal points for low dopant concentrations.

It is possible to fit the measured Fermi surface using Eq. (11.1). Such a fit is shown for an optimally doped sample on the right hand side of Fig. 11.7 by a yellow line. Only recently, due to the improved resolution, the bilayer splitting in HTSCs has been resolved [38, 39], while in low-resolution data the non-detection of this splitting was ascribed to a strong incoherence of the electronic states close to $(\pi, 0)$. From calculations of the energy dependence of the matrix element in Eq. (11.5) [40, 41] and from systematic photon-energy-dependent measurements (see below) we know that for the photon energy

$h\nu = 21.2 \text{ eV}$ the matrix element for the bonding band is more than a factor 2 larger than for the antibonding band. Therefore, we see in Fig. 11.7 mainly the Fermi surface of the bonding band. Utilizing other photon energies, the bilayer splitting can be clearly resolved, even for UD samples [36]. The red rounded squares in Fig. 11.7 illustrates the Fermi surface of the antibonding band. From the evaluation of the area of the Fermi surface and taking into account the bilayer splitting it is possible to derive the hole concentration which nicely agrees with those values derived from T_c using the universal relation, mentioned above. This is an important result supporting the validity of Luttinger's theorem (the volume of the Fermi surface should be conserved upon switching on the interactions) within the studied concentration range. Finally, we mention the existence of a shadow Fermi surface which corresponds to a (π, π) shifted (normal) Fermi surface in the Fermi surface data, shown in Fig. 11.7. After its first observation [42], it was believed to occur due to the emission of spin fluctuations. More recent measurements indicate that its origin is related to structural effects [43].

Now we come back to the determination of the bare-particle band structure. Assuming that the self-energy effects at E_F are negligible (which is supported by the experimental result that the Luttinger theorem is not violated in the concentration range under consideration), it is possible to obtain information on the unrenormalized bandstructure from the Fermi surface. By fitting the Fermi surface with a tight-binding bandstructure, one obtains relative values of the hopping integrals, i.e., the hopping integrals t' , t'' , and t_\perp normalized to t . To obtain the absolute values we have measured the spectral function along the nodal direction. From the measured widths at constant energies one can derive the imaginary part of the self-energy function. Performing a Kramers–Kronig transformation, it is possible to derive the real part of Σ and using Eq. (11.7) it is possible to calculate the bare-particle dispersion from $\epsilon_{\mathbf{k}} = E_M - \Sigma'$ where E_M is the measured dispersion (see Sect. 11.5). In this way [44] the absolute values of the hopping integrals for an UD and an OD sample has been obtained (see Table 11.2).

Table 11.2. Tight-binding parameters for an underdoped and overdoped $(\text{Bi,Pb})_2\text{Sr}_2\text{CaCu}_2\text{O}_{8+\delta}$ sample

| Sample | $t(\text{eV})$ | $t'(\text{eV})$ | $t''(\text{eV})$ | $t_\perp(\text{eV})$ | $\Delta\epsilon$ |
|---------|----------------|-----------------|------------------|----------------------|------------------|
| UD 77 K | 0.39 | 0.078 | 0.039 | 0.082 | 0.29 |
| OD 69 K | 0.40 | 0.090 | 0.045 | 0.082 | 0.43 |

A second way to determine the bare-particle bandstructure is to evaluate the anisotropic plasmon dispersion which was measured by electron energy-loss spectroscopy for momentum transfers parallel to the CuO_2 planes [45, 46]. This plasmon dispersion is determined by the projection of the Fermi velocity

on the plasmon propagation directions, which could be varied in the experiment. Since the (unscreened) plasmon energy is at about 2 eV, these excitations are considerably higher than the renormalization energies (see Table 11.1) and therefore the plasmon dispersion is determined by the unrenormalized, averaged Fermi velocity. It is thus possible to fit the momentum dependence of the averaged Fermi velocity by a tight-binding bandstructure. Similar hopping integrals as those shown in Table 11.2 were obtained for an optimally doped sample. Of course no information on the bilayer splitting could be obtained from those measurements.

Finally, a third way to obtain the bare-particle bandstructure is to look at the LDA bandstructure calculations [11]. It is remarkable that the tight-binding parameters, obtained from a tight-binding fit of the LDA bandstructure, are very similar to those given in Table 11.2.

11.5 The Dressing of the Charge Carriers at the Nodal Point

The dynamics of the charge carriers with momentum close to the nodal point determine the transport properties in the normal state. This is particularly the case in the UD region, where a pseudogap opens along the other directions. In order to obtain information on the dressing of the charge carriers at the nodal point, we performed measurements with \mathbf{k} parallel to the $(\Gamma - (\pi, \pi))$ direction (see Fig. 11.2(d)). In Fig. 11.8(a) we show the spectral function $A(E, k)$ in a false-color scale together with the bare-particle dispersion ϵ_k [47]. Already without a quantitative analysis, one can learn important facts from a simple visual inspection of Fig. 11.8(a). We clearly see that there is a strong mass renormalization over an energy range which extends up to at least 0.4 eV which is much larger than the energy of the highest phonon modes $E_{ph} = 90$ meV in these compounds [48] (for similar investigations see the contributions by Johnson and Valla and Takahashi et al. in this volume). In these normal state data the measured dispersion (red line) indicates a “soft” kink at about 70 meV but comparing the measured spectral function with that calculated for a single Einstein mode (see Fig. 11.4(c)) one realizes a clear difference. While in the one-mode model there is a sudden change of the k -dependent width from a resolution broadened delta-function to a larger width determined by the constant Σ'' , in the experimental data there is a continuous increase of the width (at constant energy) with increasing binding energy. This clearly excludes the interpretation in terms of a coupling to a single phonon line and indicates that the dominant part of the renormalization must be due to a coupling to an electronic continuum. More information can be obtained by a quantitative analysis of the data, namely the extraction of the self-energy function. As described in Subsect. 11.3.2, Σ' can be derived from the difference between the bare-particle dispersion and the measured dispersion, as determined from a fit of the data by a Lorentzian at constant

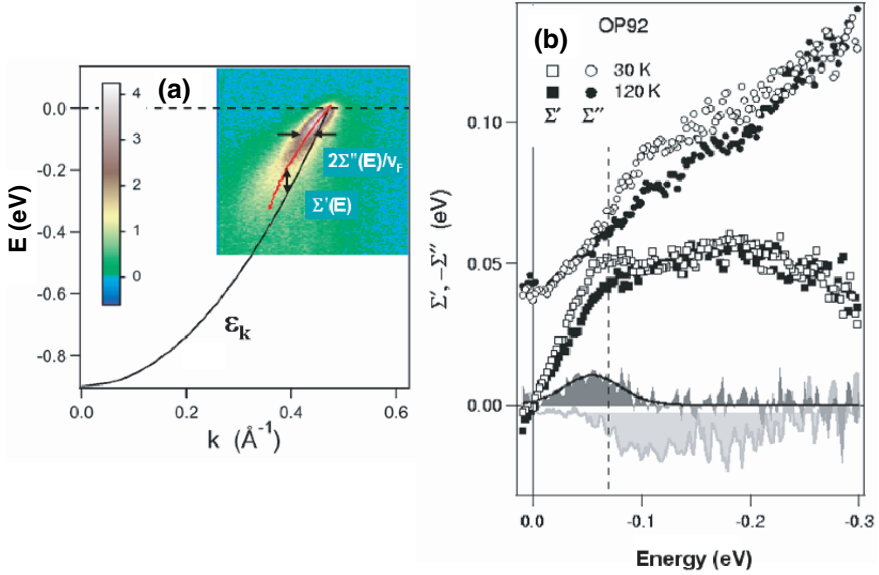


Fig. 11.8. ARPES data of optimally doped $(\text{Bi,Pb})_2\text{Sr}_2\text{CaCu}_2\text{O}_{8+\delta}$ for \mathbf{k} along to the nodal direction. (a) spectral function (in false-color scale) at $T = 130$ K together with the bare particle dispersion ϵ_k (black line). The red line gives the dispersion derived from constant E cuts; (b) Real (squares) and negative imaginary (circles) part of the self-energy function at $T = 30$ K (open symbols) and $T = 120$ K (closed symbols). Dark shaded area: difference of the real part between the two temperatures. Light shaded area: negative difference of the imaginary part between the two temperatures

energy and taking the maximum. From the same fit the width (FWHM) of the Lorentzian, Γ_k , yields $\Sigma'' = \hbar\Gamma_k v_F/2$.

In Fig. 11.8(b) we show Σ' and Σ'' of an optimally doped BiPb2212 crystal measured in the superconducting state at $T = 30$ K and in the normal state at $T = 130$ K [49]. The data can be analyzed in terms of 3 different scattering channels. The first channel related to elastic scattering from the potential of the dopant atoms and possibly also from defects at the surface can explain about 20% the offset of Σ'' at zero energy. The other 80% of the offset are due to the finite momentum resolution. The second scattering channel in the normal state can be related to a coupling to a continuum of excitations extending up to about 350 meV. This leads in the normal state to a marginal Fermi-liquid behavior (see Subsect. 11.3.2): an almost linear energy dependence of the scattering rate and at low temperatures an energy dependence of Σ' close to $E \ln E$. The continuum to which the charge carriers couple has a cut-off energy for Σ' of about 350 meV. It is remarkable that this energy is close to the energy of twice the exchange integral, $J = 180$ meV. Assuming a coupling of the charge carriers to magnetic excitations [50] in a simple approximation [30]

the self-energy function can be calculated by a convolution of the bare particle Greens function G_0 and the energy and momentum dependent magnetic susceptibility χ . This means $\Sigma = g^2(G_0 \otimes \chi)$ where g is a coupling constant. For a two-dimensional magnet it is expected that χ extends up to an energy of $2J$ and therefore if the self-energy is determined by magnetic excitations also Σ' should have a cutoff at that energy. This would support the interpretation of the continuum in terms of magnetic excitations. In this context one should mention recent ARPES measurements of an Fe film on W, where also a strong renormalization well above the phonon energies has been detected which was interpreted in terms of a coupling to magnetic excitations [51]. On the other hand the cutoff energy in Σ' may be also related to the finite width of the Cu-O band.

The third scattering channel exists mainly below T_c and its intensity is getting rather weak at higher temperatures. It causes a peak in Σ' near 70 meV and an edge in Σ'' at about the same energy. This leads to a pronounced change of the dispersion at the nodal point at ~ 70 meV which was previously termed the “kink” [52]. The differences between the self-energy functions $\Delta\Sigma'$ and $\Delta\Sigma''$ when going from 30 K to 130 K are plotted in Fig. 11.8(b) by shaded areas. Both are typical of a self-energy function determined by a single bosonic mode. The energy of the mode may be either ~ 70 meV, when the nodal point is coupled to gap-less other nodal states or ~ 40 meV when they are coupled to states close to the antinodal point which in the superconducting state have a gap of 30 meV. A bosonic mode near 40 meV can be related to the magnetic resonance mode, first detected by inelastic neutron scattering experiments [53], a collective mode (spin exciton) which is formed inside the spin gap of 2Δ and which decays into single-particle excitations above T_c because of the closing of the gap. The mode energy $\Omega_0 = 40$ meV together with a gap energy $\Delta = 30$ meV yields a kink energy of 70 meV thus explaining the kink by a coupling of the antinodal point to the nodal point. Previous ARPES, optical, and theoretical studies [54–56] have been interpreted in terms of this magnetic resonance mode. On the other hand, theoretical work [57] has pointed out that because of kinematic constraints a coupling of the antinodal point to the nodal point via the 40 meV magnetic resonance mode should not be possible. Recently a new magnetic resonance mode (the Q^* mode) near 60 meV has been detected [58, 59] which may explain the above mentioned coupling between nodal points.

In principle the appearance of a sharper kink in the superconducting state and a *decrease* of the scattering rate in the superconducting state [60] has been also explained by the opening of a superconducting gap in the continuum [30]. On the other hand, the data shown in Fig. 11.8(b) could indicate that in the superconducting state when compared with the normal state, there is an *additional* scattering channel and not a *reduction* of the scattering rate.

In the following we discuss the doping and temperature dependence of the renormalization effects at the nodal point. In Fig. 11.9(a) we show the doping dependence of the real part of the self-energy function above T_c [47].

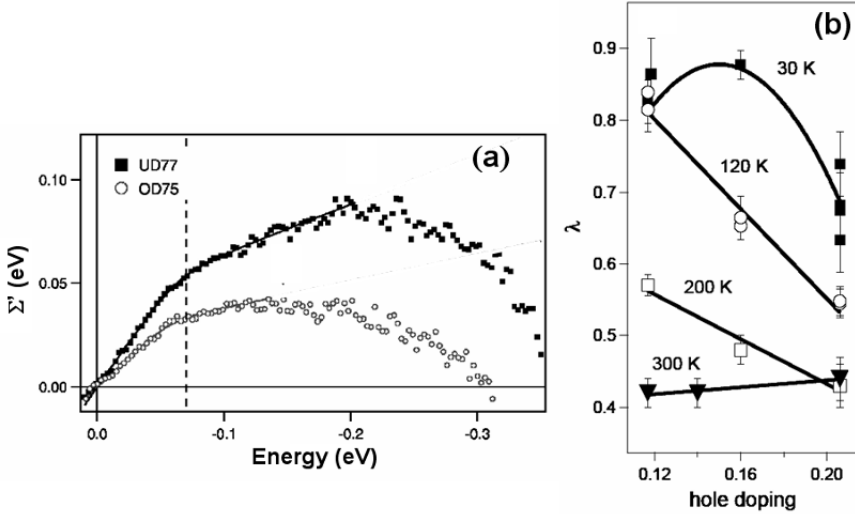


Fig. 11.9. (a) Real part of the self-energy function, Σ' , for two $(\text{Bi,Pb})_2\text{Sr}_2\text{CaCu}_2\text{O}_{8+\delta}$ samples at $T = 130\text{ K}$ at the nodal point. UD77: underdoped with $T_c = 77\text{ K}$, OD75: overdoped with $T_c = 75\text{ K}$; (b) coupling constant λ at the nodal point as a function of hole concentration for various temperatures

Here the contributions from the third scattering channel, the coupling to a single bosonic mode, have almost disappeared and mainly a coupling to the continuum is observed. A rather strong doping dependence is realized. In the UD sample Σ' is much larger and extends to much higher energies compared to the OD sample. This could support the assumption that the continuum is related to magnetic excitations, which increase when approaching the Mott–Hubbard insulator. From the slope at zero energy (see Subsect. 11.3.2), λ values could be derived which are summarized in Fig. 11.9(b). The strong doping dependence of λ in the normal state questions the postulation that independent of the dopant concentration there is a universal Fermi velocity [61].

In the normal state λ decreases with increasing hole concentration and increasing temperature. This is expected in the scenario of a coupling to a continuum of overdamped spin excitations since for the susceptibility of these excitations a similar doping and temperature dependence is expected. At 300 K, λ is almost independent of the hole concentration. Possibly there the contribution from the coupling to a continuum of magnetic excitations has become smaller than the contributions from electron–hole excitations without spin reversal. The temperature dependence of the coupling constant at lower hole concentrations is consistent with the marginal Fermi-liquid model, since there at high temperatures the low-energy properties are no more determined by the energy dependence and therefore λ should decrease with increasing

temperature. This is in stark contrast to the normal Fermi-liquid behavior which is observed in the OD sample (see below).

In the superconducting state there is an additional increase of λ , the concentration dependence of which is quite different from that in the normal state. This clearly indicates once more the existence of a new additional scattering channel below T_c .

The scattering rate being linear in energy for the OP doped sample at 130 K transforms *continuously* into a more quadratic one both in the normal and the superconducting state [62, 63]. This indicates that both the second and the third scattering channel decrease with increasing hole doping, which is expected in the magnetic scenario. The doping dependence shows in the normal state a transition from a marginal Fermi-liquid behavior to a more normal Fermi-liquid behavior at high hole concentrations. The quadratic increase in energy (see Subsect. 11.3.2) of Σ' is determined by the coefficient $\beta = 1.8 \text{ (eV)}^{-1}$. This coefficient is much larger than the value 0.14 derived for electrons forming the Mo(110) surface states [64]. This indicates that even in OD HTSCs correlation effects are still important and electron–electron interactions and possibly still the coupling to spin fluctuations are strong.

The strong doping and temperature dependence of the additional (bosonic) channel is difficult to explain in terms of phonon excitations. We therefore offered for the additional third scattering channel an explanation in terms of a coupling to a magnetic neutron resonance mode, which only occurs below T_c . Finally we mention that an explanation of the extension of the renormalization to high energies in terms of a multi-bosonic excitation is very unlikely. A λ value below 1, which corresponds to a quasi-particle spectral weight Z^{-1} larger than 0.5 would not match with a coupling to polaronic multi-bosonic excitations.

11.6 The Dressing of the Charge Carriers at the Antinodal Point

Most of the ARPES studies in the past were focused on the nodal point, where narrow features in (E, \mathbf{k}) space have been detected, indicating the existence of quasi-particles far down in the underdoped or even slightly doped region. On the other hand the antinodal point is of particular interest concerning the superconducting properties, since in the d-wave superconductors the superconducting order parameter has a maximum at the antinodal point [12]. The region near the $(\pi, 0)$ point has been always much more difficult to investigate due to complications of the bilayer splitting, which could not be resolved by ARPES for 15 years. On the other hand, as mentioned above, only with bilayer systems of the Bi-HTSC family the entire superconducting range from the UD to the OD region can be studied. Thus due to the existence of two Fermi surfaces and two bands close to the Fermi level near $(\pi, 0)$, with a reduced resolution only a broad distribution of spectral weight

could be observed, leading to the conclusion that in this (E, k) range very strong interactions appear causing a complete incoherence of the dynamics of charge carriers [65]. Moreover, in the superconducting state, very early a peak-dip-hump structure has been observed for all dopant concentrations which in analogy to the tunnelling spectra in conventional superconductors, was interpreted as a strong coupling to a bosonic excitation [65]. This picture partially changed with the advent of the improved experimental situation.

First of all it has been shown by photon-energy dependent measurements in the range $h\nu = 20\text{--}60\text{ eV}$ using synchrotron radiation [66,67] that the peak-dip-hump structures strongly change as a function of the photon energy. This indicated that the matrix element in Eq. (11.5) has a different photon energy dependence for the bonding and the antibonding band at $(\pi, 0)$. This experimental observation was confirmed by calculations of the matrix element using LDA bandstructure calculations [40,41]. It turned out that the peak-dip-hump structure in the OD sample was dominated by the bilayer splitting, i.e. the peak is caused by the antibonding band and a hump is caused by the bonding band. In the UD range the complicated spectral shape could be traced back to a superposition of the bilayer effects and strong renormalization effects in the superconducting state. In this situation, only momentum-dependent measurements [68–70] along the $(\pi, \pi) - (\pi, -\pi)$ line could separate the two effects. In Fig. 11.10 a collection of our ARPES data along this direction, centered around the $(\pi, 0)$ point, is shown as a function of the dopant concentration in the superconducting state ($T = 30\text{ K}$). In the lowest row, normal state data ($T = 120\text{ K}$) are also shown for the UD sample. In the upper left corner the data for an OD sample clearly show the splitting into a bonding and an antibonding band related to four Fermi-surface crossings and two saddle points as expected from the tight-binding bandstructure calculations, shown in Fig. 11.2(a) taking into account the bilayer splitting visualized in Fig. 11.2(d). Looking in the same column at the low temperature data of the OP and UD sample the two bands are no more resolved. As mentioned before the matrix element for the excitation of the 2 bands is strongly photon energy dependent and it was shown [40, 41, 66, 67] that the spectra in the first column which were taken at $h\nu = 38\text{ eV}$ represent mainly the bonding band with some contributions from the antibonding band. The data in the second column were taken with $h\nu = 50$ (or 55) eV and have almost pure antibonding character. Subtracting the second column from the first column yields almost the pure spectral weight from the bonding band. Using this procedure one clearly recognizes that even in the UD samples the bonding and the antibonding band can be well separated. In the superconducting state (first 3 rows) these data show strong changes upon reducing the dopant concentration. The bonding, and most clearly seen, the antibonding band move further and further below the Fermi level, indicating the reduction of holes. In the bonding band of the OD crystal almost no kink is observed but in the OP sample a very strong kink is realized, disclosed by the appearance of a flat dispersion between the gap energy at about $\sim 30\text{ meV}$ and the branching energy of $\sim 70\text{ meV}$ followed

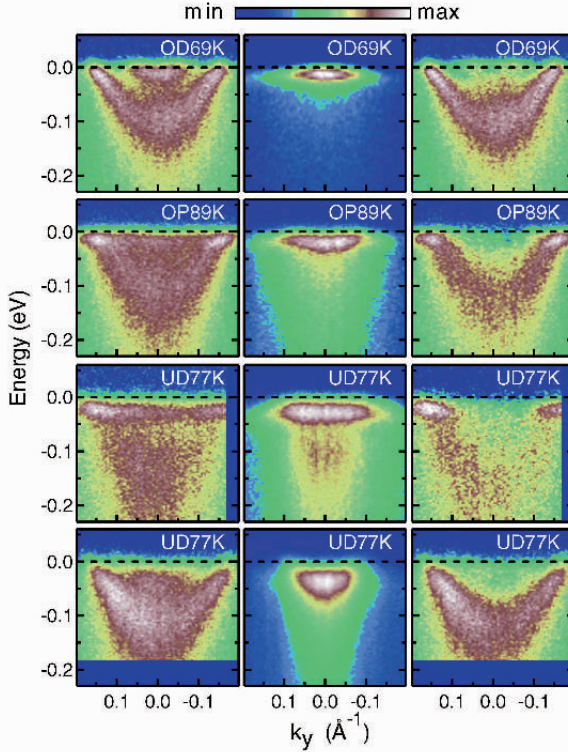


Fig. 11.10. ARPES intensity plots as a function of energy and wave vector along the $(\pi, \pi) - (\pi, -\pi)$ direction of overdoped (OD), optimally doped (OP) and underdoped (UD) $(\text{Bi,Pb})_2\text{Sr}_2\text{CaCu}_2\text{O}_{8+\delta}$ superconductors taken at $T = 30$ K (upper 3 rows). Zero corresponds to the $(\pi, 0)$ point. Fourth row: data for an UD sample taken at $T = 120$ K. *Left column:* data taken with a photon energy $h\nu = 38$ eV, at which the signal from the bonding band is maximal. *Middle column:* data taken at $h\nu = 50$ eV (or 55 eV), where the signal from the antibonding band is dominant. *Right column:* subtraction of the latter from the former yielding the spectral weight of the bonding band

by a steeper dispersion and a strong broadening. The strong renormalization effects increase even further when going from the OP doped sample to the UD sample. Remarkably, the renormalization effects (with the exception of the pseudogap) described above, completely disappear in the normal state as can be seen in the fourth row where data from an UD sample, taken at 120 K, are shown. As in the OD sample, a normal dispersion without a kink is now detected for the bonding band. Also for the antibonding band there is a transition from a flat band at low temperatures to a dispersive band above T_c . A comparison with the bare-particle band structure (not shown) indicates that there is reduction of the bandwidth by a factor of about 2 which means that there is a λ^w of about 1 in the normal state. A renormalization corresponding

to a λ^w of about 1 is also detected above the branching energy near $(\pi, 0)$ in the superconducting state. This bandwidth renormalization in the range of the antinodal point is similar to that one at the nodal point and is probably also related to a coupling to a continuum of magnetic excitations.

In Fig. 11.11(a) we show an ARPES intensity distribution of the antibonding band near k_F measured with a photon energy $h\nu = 50$ eV along the $(1.4\pi, \pi) - (1.4\pi, -\pi)$ line for OP Pb-Bi2212 at 30 K. At this place in the second Brillouin zone the bare particle dispersion of the antibonding band reaches well below the branching energy $E_B = 70$ meV. Therefore, contrary to the data shown in Fig. 11.10 (second row, second column), which were taken along the $(\pi, \pi) - (\pi, -\pi)$ line, the branching into two dispersive arms can be clearly realized. The data in Fig. 11.11(a) together with those shown in Fig. 11.10 (second row, third column) for the bonding band, when compared with the model calculations shown in Fig. 11.5, clearly show that the dominant renormalization effect in the superconducting state is a coupling to a bosonic mode [60, 71].

To obtain more information about the renormalization and the character of the mode, the spectral function was analyzed quantitatively [72]. Cutting the measured intensity distribution of the bonding band (see Fig. 11.10) at k_F yields the peak-dip-hump structure shown in Fig. 11.11(b). From the peak

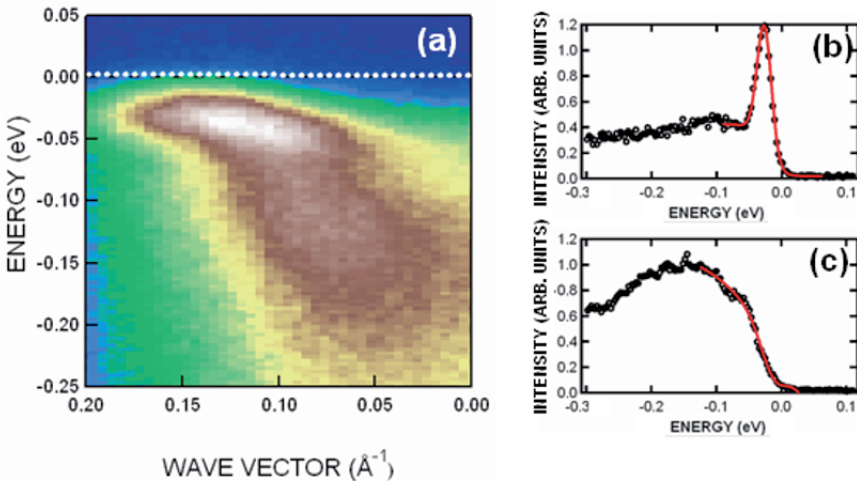


Fig. 11.11. (a) Spectral function for k -values near the $(1.4\pi, \pi) - (1.4\pi, -\pi)$ direction of the OP $(\text{Bi,Pb})_2\text{Sr}_2\text{CaCu}_2\text{O}_{8+\delta}$ superconductor taken at $T = 30$ K. Zero corresponds to the $(1.4\pi, 0)$ point. The data were taken with a photon energy $h\nu = 50$ eV in order to maximize the intensity of the antibonding band; (b) constant- k cut of the spectral weight of the bonding band (see Fig. 11.10, optimally doped sample, $T = 30$ K) at k_F ; (c) cut of the data at about one third of k_F (starting from $(\pi, 0)$)

energy one can derive a superconducting gap energy of $\Delta = 30$ meV. Cutting the data at about $1/3$ of k_F (starting from $(\pi, 0)$) yields the spectrum shown in Fig. 11.11(c). There the coherent peak is strongly reduced and in the framework of a one-mode model, the threshold after the coherent peak, derived from a fit of the spectrum, yields the branching energy $\Omega_0 + \Delta = 70$ meV. Another way to obtain the branching energy is to determine the threshold of Σ'' which can be obtained by fitting the spectral weight of constant energy cuts using Eq. (11.10). From this, the branching energy $\Omega_0 + \Delta = 70$ meV can be derived. From fits of constant energy cuts just below the branching energy the parameter $\Sigma''(-\infty) \sim 130$ meV can be obtained which is also a measurement of the coupling of the charge carriers to a bosonic mode (see Subsect. 11.3.2).

Important information comes from the dispersion between the gap energy and the branching energy. Originally [68] the data were fitted using Eq. (11.12) yielding λ values as a function of the dopant concentration shown in Fig. 11.12. However, as pointed out in Subsect. 11.3.3, the situation in HTSCs is quite different from conventional superconductors. In the former Ω_0 is not much larger than Δ and therefore the function $Z(E)$, from which λ is derived, is energy dependent. Furthermore, as shown in Subsect. 11.3.3 the λ values, evaluated in this way, depend on the gap energy. In the one-mode model the gap energy dependence of λ is determined by the factor $(\Omega_0 + \Delta)/\Omega_0$. Therefore it is questionable whether those λ values are a good measure of the coupling strength to a bosonic mode. More recently [72], we have fitted the dispersion of the coherent peak of an OP doped sample using the full Eq. (11.11) taking into account the above mentioned band renormalization by a factor of 2 using a $\lambda^w \sim 1$. From the derived $Z(E)$ in the superconducting state, $Z(E)$ in the normal state could be calculated by setting Δ to zero and then a total coupling constant $\lambda_n^t = 3.9$ could be obtained which is composed of a $\lambda_n^b = 2.6$ due to the coupling to the bosonic mode and a $\lambda_n^w = 1.3$ from

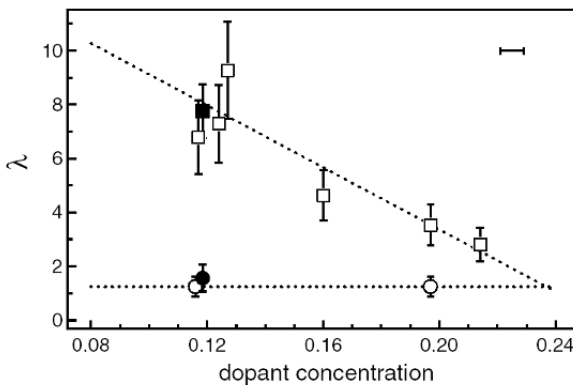


Fig. 11.12. The coupling strength parameter λ at the antinodal point as a function of doping concentration. *Squares*: superconducting state; *circles*: normal state; *open (solid) symbols*: bonding (antibonding) band

the band renormalization. It is interesting that this value is close to the value derived using Eq. (11.12). The reason for this is that the reduction due to the energy dependence of Z is partially compensated by the transformation into the normal state. A first estimate shows that the values at other dopant concentrations are also not drastically changed.

One may argue that those very large λ -values are unphysical and meaningless because, in the case of electron–phonon coupling, lattice instabilities may be expected. On the other hand also another measure of the coupling strength, the imaginary part of the self-energy function above the branching energy is very large. From $\Sigma''(-\infty) = 130$ meV and $\Omega_0 = 40$ meV one obtains (see Sect. 11.3.2) $\lambda = \Sigma''(-\infty)/(\pi\Omega_0/2) = 2.1$ which is not far from the above given value $\lambda_n^b = 2.6$ for the coupling to the bosonic mode derived from the dispersion.

It is interesting to compare the present values of $\lambda_n^b = 2.6$ and $\Sigma''(-\infty) = 130$ meV derived for an OP HTSC in the superconducting state with those obtained for the electron–phonon coupling of surface electrons on a Mo(110) surface ($\lambda_n^b = 0.42$ and $\Sigma''(-\infty)_{el-ph} = 30$ meV) [23]. So both parameters are for the HTSC a factor 4–6 larger than for the Mo(110) surface. This indicates that in the HTSCs in the superconducting state there is really an anomalous strong coupling to a bosonic mode, which manifests itself both in the high coupling constant and in the high scattering rates above the branching energy. Finally it is remarkable that there is no indication of a multibosonic excitation comparable to that in the undoped cuprates [26, 27] since in that case, taking the above derived λ^b values, the intensity of the coherent state relative to the incoherent states should be strongly reduced in disagreement with the data shown in Figs. 11.10 and 11.11.

In Fig. 11.13 we show the renormalization of the antibonding band in the superconducting state for an OP sample when going from the antinodal point to the nodal point [73]. By looking at the dispersion close to E_F the

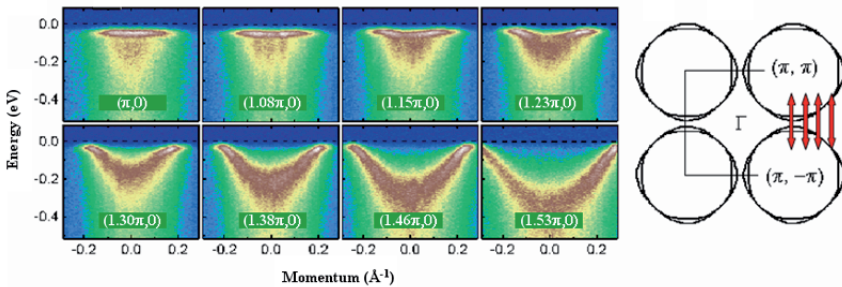


Fig. 11.13. Intensity distribution for cuts in the Brillouin zone indicated in the right-hand sketch of the optimally doped $(\text{Bi,Pb})_2\text{Sr}_2\text{CaCu}_2\text{O}_{8+\delta}$ superconductor taken at $T = 30$ K. *Upper left panel:* antinodal point. *Lower right panel:* nodal point. The data were taken with a photon energy $h\nu = 50$ eV in order to maximize the intensity of the antibonding band

renormalization is large at the antinodal point and it is much weaker at the nodal point. This is in line with a strong coupling to a mode which is related to a high susceptibility for a wave vector (π, π) which leads to a coupling between antinodal points.

This leads to the above mentioned spin fluctuation scenario, in which below T_c , the opening of the gap causes via a feed-back process the appearance of a magnetic resonance mode, detected by inelastic neutron scattering [53]. This mode has a high spin susceptibility at the wave vector (π, π) , the energy is ~ 40 meV, and as mentioned above it exists only below T_c . Thus from the measurements of the spectral function around $(\pi, 0)$, in particular from the energy, the momentum, and the temperature dependence we conclude that the mode to which the charge carriers at the antinodal point so strongly couple, is the magnetic resonance mode. In a recent theoretical work [56] it was pointed out that according to magnetic susceptibility measurements using inelastic neutron scattering the magnetic resonance mode couples the antibonding band predominantly to the bonding band and vice versa. This means only the odd susceptibilities χ_{AB} and χ_{BA} are large and the even susceptibilities χ_{AA} and χ_{BB} are small. There is no coupling via the resonance mode within a band. It is remarkable that the coupling of the bonding band to the resonance mode starts in the OD region near 22% doping when the saddle point of the antibonding band just crosses the Fermi level (see Fig. 11.12). The result that in the UD region λ is similar for both bands is understandable, since the Fermi velocities and therefore the density of states and the odd susceptibilities χ_{AB} and χ_{BA} should be comparable. This scenario is supported by recent measurements of the energy dependence of the different scattering rates of the bonding and the antibonding band close to the nodal point [74]. Similar data have been recently presented for the system $\text{YBa}_2\text{Cu}_3\text{O}_7$ [75]. Furthermore, recently our group has observed large changes of the renormalization effects at the nodal and the antinodal point upon substituting 1 or 2% of the Cu ions by nonmagnetic Zn ($S = 0$) or magnetic Ni ($S = 1$), respectively [76]. These strong changes also strongly support the magnetic scenario since this substitution of a very small amount of the Cu ions should not change the coupling of the charge carriers to phonons. On the other hand we do not want to conceal that there are also interpretations of the above discussed bosonic mode in terms of phonon excitations [77].

At the end of this Section we would like to mention some ARPES results on the spectral function in the pseudogap region [78]. The pseudogap is one of the most remarkable properties of HTSCs in the UD region above T_c . In Fig. 11.14 we compare the dispersion along the $(\pi, 0) - (\pi, -\pi)$ direction close to the antinodal point of an UD sample in the superconducting and in the pseudogap state. In the superconducting state one realizes the characteristic BCS-Bogoliubov-like back-dispersion at \mathbf{k}_F . In the pseudogap state no more a bending back of the dispersion is observed. Instead the spectral weight fades when the binding energy approaches the gap energy. This is in line with the observed disappearance of the coherence peak in tunnelling spectra of HTSCs

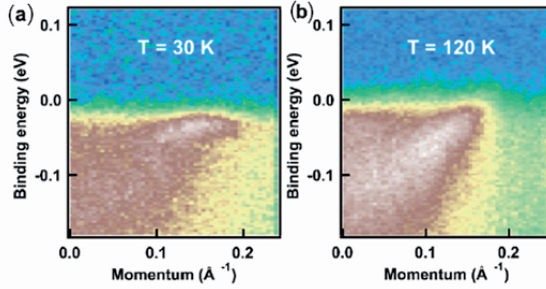


Fig. 11.14. Intensity distribution near the antinodal point along the $(\pi, 0) - (\pi, -\pi)$ direction of an underdoped $(\text{Bi,Pb})_2\text{Sr}_2\text{CaCu}_2\text{O}_{8+\delta}$ crystal with $T_c = 77$ K. The photon energy has been chosen to be 38 eV in order to suppress the antibonding band. (a) superconducting state; (b) pseudogap state

in the pseudogap phase [79]. The experimental observation of this behavior was explained in terms of phase fluctuations of the superconducting order parameter. The BCS wave function is a coherent superposition of wave functions with different number of electrons, N , and usually also a phase factor $e^{i\phi}$ is introduced. This leads to a general uncertainty relation for the particle number and the phase: $\Delta N \Delta \phi \geq 1$ [80]. In the superconducting state at $T = 0$ where there is a large phase stiffness, i.e., $\Delta \phi = 0$, the particle number is completely uncertain leading to a large particle-hole mixing and thus to a large back-dispersion. With increasing temperature, the phases get completely uncorrelated and one obtains $\Delta N = 0$. Then the back-dispersion must disappear. In this way a crossover from a BCS-like phase-ordered bandstructure to a completely new phase-disordered pseudogap bandstructure is obtained.

11.7 Conclusions

In this chapter we presented part of our ARPES results on HTSCs. They were obtained with an energy and a momentum resolution of 8-25 meV and 0.015 \AA^{-1} . This is at present the state-of-the-art ARPES when reasonable intensities are used during the measurements. Using this resolution, a lot of information on the dressing of the charge carriers in HTSCs at different k-points in the Brillouin zone has been obtained during the last 10 years. It will be really one of the big challenges of experimental solid state physics to enter in the range of sub-1meV-resolution in *angle-resolved* photoemission spectroscopy. In the next 10 years it is predictable that there will be a further improvement of the energy resolution by one order of magnitude for angle-resolved measurements. It can be anticipated that further interesting results on the dressing and possibly also on the pairing mechanism in HTSCs can be realized.

Acknowledgements

We acknowledge financial support by the DFG Forschergruppe under Grant No. FOR 538. One of the authors (J.F.) appreciates the hospitality during his stay at the Ames Lab and thanks for the critical reading of the manuscript by D. Lynch. We thank R. Follath, T.K. Kim, S. Legner, and K.A. Nenkov for fruitful collaboration. In particular we thank Mark Golden for his contributions in the early stage of the project. Finally we acknowledge helpful discussions and collaboration with colleagues from theory: A.V. Chubukov, T. Eckl, M. Eschrig, and W. Hanke.

References

1. A. Einstein: Ann. d. Phys. **31**, 132 (1905)
2. H. Hertz: Ann. d. Phys. **17**, 983 (1887)
3. G. W. Gobeli et al.: Phys. Rev. Lett. **12**, 94 (1964)
4. G. Bednorz and K. A. Müller: Z. Phys. B **64**, 189 (1986)
5. J. Zaanen et al.: Phys. Rev. Lett. **64**, 189 (1986)
6. D. W. Lynch and C. G. Olson: *Photoemission Studies of High-Temperature Superconductors* (Cambridge University Press 1999), pp 1–432
7. A. Damascelli et al.: Rev. Mod. Phys. **75**, 473 (2003)
8. J. C. Campuzano et al.: Photoemission in the High- T_c Superconductors. In: *Physics of Superconductors*, vol II, ed by K. H. Bennemann and J. B. Ketterson (Springer, Berlin Heidelberg New York 2004), pp 167–273
9. T. Timusk: Rep. Progr. Phys. **62**, 61 (1999) **75**, 473 (2003)
10. C. M. Varma: Phys. Rev. B **55**, 14554 (1997)
11. O. K. Andersen et al.: J. Phys. Chem. Solids **56**, 1573 (1995)
12. H. Ding et al.: Phys. Rev. B **54**, R9678 (1996)
13. S. V. Borisenko et al.: Phys. Rev. B **66**, 140509(R) (2002)
14. A. A. Kordyuk et al.: Phys. Rev. B **70**, 214525 (2004)
15. N. Nücker et al.: Phys. Rev. B **37**, 6827 (1988)
16. S. Hüfner: *Photoelectron Spectroscopy* (Springer, Berlin Heidelberg New York 1996) and references therein.
17. G. D. Mahan: *Many-Particle Physics* (Plenum Press, New York 1990)
18. L. Hedin and S. Lundquist: Solid State Physics **23**, 1963 (1969)
19. C. O. Almbladh and L. Hedin: Beyond the one-electron model in *Handbook of Synchrotron Radiation*, vol 1b, ed by E. E. Koch (North Holland, Amsterdam 1983), pp 607–904
20. C. M. Varma et al.: Phys. Rev. Lett. **63**, 1996 (1989)
21. D. Pines and P. Nozières: *The Theory of Quantum Liquids*, vol 1, (W. A. Benjamin, New York 1966), p. 64
22. M. Imada et al.: Rev. Mod. Phys. **70**, 1039 (1998)
23. T. Valla et al.: Science **285**, 2110 (1999)
24. C. Hodges et al.: Phys. Rev. B **4**, 302 (1971)
25. S. Engelsberg and J. R. Schrieffer: Phys. Rev. **131**, 993 (1963)
26. K. M. Shen et al.: Phys. Rev. Lett. **93**, 267002 (2004)
27. O. Rösch and O. Gunnarsson: Phys. Rev. Lett. **92**, 146403 (2004)

28. Y. Nambu: Phys. Rev. **117**, 648 (1960)
29. D. J. Scalapino, in *Superconductivity*, vol. 1, ed. R. D. Parks (Marcel Decker, New York 1969), p. 449
30. A. V. Chubukov and M. R. Norman: Phys. Rev. B **70**, 174505 (2004)
31. N. Martensson et al.: Journal of Electron Spectroscopy and Related Phenomena **70**, 117 (1994)
32. *Handbook on Synchrotron Radiation*, vol 1-4, ed by E. E. Koch et al (North Holland, Amsterdam 1983–1991)
33. R. Follath: Nucl. Instrum. Meth, Phys. Res. A **467–468**, 418 (2001)
34. S. V. Borisenko et al.: Phys. Rev. Lett. **84**, 4453 (2000)
35. S. Legner et al.: Phys. Rev. B **62**, 154 (2000)
36. A. A. Kordyuk et al.: Phys. Rev. B **66**, 014502 (2002)
37. J. L. Tallon et al.: Phys. Rev. B **51**, 12911 (1995)
38. D. L. Feng et al.: Phys. Rev. Lett. **86**, 5550 (2001)
39. Y.-D. Chuang et al.: Phys. Rev. Lett. **87**, 117002 (2001)
40. A. Bansil and M. Lindroos, Phys. Rev. Lett. **83**, 5154 (1999)
41. J. D. Lee and A. Fujimori, Phys. Rev. Lett. **87**, 167008 (2001)
42. P. Aebi et al.: Phys. Rev. Lett. **72**, 2757 (1994)
43. A. Koitzsch et al.: Phys. Rev. B **69**, 220505(R) (2004)
44. A. A. Kordyuk et al.: Phys. Rev. B **67**, 064504 (2003)
45. N. Nücker et al.: Phys. Rev. B **44**, 7155 (1991)
46. V. G. Grigorian et al.: Phys. Rev. B **60**, 1340 (1999)
47. A. A. Kordyuk et al.: Phys. Rev. B **71**, 214513 (2005)
48. L. Pintschovius and W. Reichardt: Neutron Scattering in Layered Copper-Oxide Superconductors. In: *Physics and Chemistry of Materials with Low Dimensional Structures*, vol 20, ed. by A. Furrer (Kluwer Academic, Dordrecht, 1998), p. 165
49. A. A. Kordyuk et al.: Phys. Rev. Lett. **97**, 017002 (2006)
50. A. Abanov et al.: Adv. Phys. **52**, 119 (2003).
51. J. Schäfer et al.: Phys. Rev. Lett. **02**, 097205 (2005)
52. P. V. Bogdanov et al.: Phys. Rev. Lett. **85**, 2581 (2000)
53. J. Rossat-Mignod et al.: Physica C **185–189**, 86 (1991); H. A. Mook et al.: Phys. Rev. Lett. **70**, 3490 (1993); H. F. Fong et al.: *ibid.* **75**, 316 (1995)
54. P. D. Johnson et al.: Phys. Rev. Lett. **87**, 177007 (2001)
55. J. Hwang et al.: cond-mat/0505302
56. M. Eschrig and M. R. Norman: Phys. Rev. Lett. **85**, 3261 (2000), Phys. Rev. Lett. **89**, 277005 (2002), Phys. Rev. B **67**, 144503 (2003)
57. A. Abanov et al.: Phys. Rev. Lett. **89**, 177002 (2002)
58. S. Pailhes et al.: Phys. Rev. Lett. **93**, 167001 (2004)
59. I. Eremin et al.: cond-mat/0409599
60. A. Kaminski et al.: Phys. Rev. Lett. **86**, 1070 (2001)
61. X. J. Zhou et al.: Nature **423**, 398 (2003)
62. A. Koitzsch et al.: Phys. Rev. B **69**, 140507(R) (2004)
63. A. A. Kordyuk et al.: Phys. Rev. Lett **92**, 257006 (2004)
64. T. Valla, A. V. Feferov et al.: Phys. Rev. Lett. **83**, 2085 (1999)
65. Z.-X. Shen and J. R. Schrieffer: Phys. Rev. Lett. **78**, 1771 (1997)
66. S. V. Borisenko et al.: Phys. Rev. Lett. **90**, 207001 (2003)
67. A. A. Kordyuk et al.: Phys. Rev. Lett. **89**, 077003 (2002)
68. T. K. Kim et al.: Phys. Rev. Lett. **91**, 167002 (2003)
69. A. D. Gromko et al.: Phys. Rev. B **68**, 174520 (2003)

70. T. Sato et al.: Phys. Rev. Lett. **91**, 157003 (2003)
71. M. R. Norman, H. Ding: Phys. Rev. B **57**, 11111 (1998)
72. J. Fink et al.: Phys. Rev. B **74**, 165102 (2006)
73. T. K. Kim: The role of inter-plane interactions in the electronic structure of high- T_c cuprates. PhD Thesis, University of Technology, Dresden (2003)
74. S. V. Borisenko et al.: Phys. Rev. Lett. **96**, 067001 (2006)
75. S. V. Borisenko et al.: Phys. Rev. Lett. **96**, 117004 (2006)
76. V. Zabolotnyy et al.: Phys. Rev. Lett. **96**, 037003 (2006)
77. T. P. Devereaux et al.: Phys. Rev. Lett. **93**, 117004 (2004)
78. T. Eckl et al.: Phys. Rev. B **70**, 094522 (2004)
79. M. Kugler et al.: Phys. Rev. Lett. **86**, 4911 (2001)
80. M. Tinkham: *Introduction to Superconductivity* (McGraw-Hill, New York, 1996)